Renewable Energy 72 (2014) 354–366

Contents lists available at ScienceDirect

Renewable Energy

journal homepage: www.elsevier.com/locate/renene

Generic ground response functions for ground exchangers in the presence of groundwater flow

Maxime Tye-Gingras, Louis Gosselin*

Department of Mechanical Engineering, Université Laval, Québec City, Québec, Canada

ARTICLE INFO

Article history:
Received 8 January 2014
Accepted 15 July 2014
Available online 9 August 2014

Keywords:
Vertical ground heat exchanger
Geothermal
Groundwater
Ground response functions

ABSTRACT

This paper describes a procedure for computing time-dependent ground response functions (G) of vertical ground exchangers in the presence of groundwater flow. The comprehensive methodology can account for multi-borehole fields and allows predicting accurately heat transfer over a large range of design parameters, ground properties and time scales. It combines two analytical models: infinite cylinder source (ICS) and moving finite line source (MFLS). A new mathematical development is introduced to enhance the computational efficiency of the G-functions with the MFLS model. The precision of the models as a function of time is verified with finite-element modeling. An application-oriented procedure allows expressing the G-functions as a function of all the variables by combining graphical tools and correlation fittings. This procedure is developed specifically to be easily implemented in borehole design methods. The G-functions obtained by this method are in good agreement ($R^2 = 0.9934$) with the analytical solution developed, over the prescribed range of variables.

1. Introduction

The market of ground coupled heat pump (GCHP) systems is currently growing fast. Vertical ground heat exchangers are among the most widely used types of ground heat exchangers. For example, they occupy around 85% of the market in the province of Québec (Canada) [1]. ASHRAE has elaborated a design procedure in order to size vertical ground heat exchangers [2]. However, several assumptions were invoked to develop this design method, one of the major being that the ground is considered as a homogeneous material with no groundwater flow. This limitation is often a source of struggles for practice engineers who design ground heat exchangers in geological environments where groundwater flow is present. In fact, ASHRAE recognized this fact, and mentioned in its handbook that "because the effect [of groundwater movement] has not been thoroughly studied, the design engineer must establish a range of design lengths" [2]. Besides, the need for suitable models accounting for groundwater advection has been expressed by Chiasson et al. [3].

Although the problem of groundwater flow has already been addressed since the 80's in a few papers on ground heat exchangers, groundwater has been largely ignored in most design procedures used by practitioners due to a lack of general data that is not "case-specific" and of easily usable tools and procedures for design. For example, in 1985, van Moeurs [4] numerically observed and characterized the evolution of the borehole heat transfer as a function of the Peclet number of the flow. However, his work was focused on a specific borefield configuration, and therefore, it was hardly applicable to a general design methodology. In 1987, Eskilson [5] developed analytical equations for solving heat transfer in the ground including groundwater advection. However, it was developed for a single borehole in steady-state only, and it actually gave the temperature at borehole mid-height instead of the average on the borehole, which required a correction factor. In 2000, Claesson and Hellstrom [6] presented accurate and fast-solving approximations to a mathematical development including the integration of the temperature over the whole depth of the borehole with groundwater flow. However, their g_{gw}-functions were valid for a single borehole only.

Since then, different attempts to investigate the effect of groundwater flow on the heat transfer around boreholes have been reported in literature. The development of analytical models considering groundwater flow was undertaken by Sutton et al. [7] and Diao et al. [8] who obtained an expression for transient and steady-state temperature rise in the ground with groundwater advection. Their models were both based on the moving infinite line heat source (MILS) theory. Molina-Giraldo et al. [9] developed the moving finite line source (MFLS) solution to account for axial effects. Recently, Cappoza et al. verified the MILS theory in a real case study and used the model for borefield simulations [10]. For their specific case, they concluded that the model was valid and considering groundwater flow could have allowed 16% savings on

* Corresponding author: Tel.: +1 418 656 7829; fax: +1 418 656 7415.
E-mail address: Louis.Gosselin@gmc.ulaval.ca (L. Gosselin).

http://dx.doi.org/10.1016/j.renene.2014.07.026
0960-1481/

Nomenclature

A	borefield aspect ratio (longest side/shortest side), [−]
B	borehole separation distance, [m]
E	error, [−] or [%]
Fo	Fourier number $\alpha_{\text{eff}}t/r_b^2$ or $\alpha_{\text{eff}}t/H^2$, [−]
G	ground function, [−]
G_N	overall ground function (for N boreholes), [−]
G_1	Ground function for a single borehole, [−]
G_{N1}	ground function due to borehole interactions, [−]
H	borehole vertical length, [m]
I	I-type Bessel function, [−]
J	J-type Bessel function, [−]
K	hydraulic conductivity, [m/s]
N	number of boreholes, [−]
Pe	Peclet number $u_{\text{eff}}r_b/\alpha_{\text{eff}}$ or $u_{\text{eff}}H/\alpha_{\text{eff}}$, [−]
T	temperature, [K, °C]
V	variable combination, [−]
Y	Y-type Bessel function, [−]
c_p	thermal capacity, [J/kg K]
k	thermal conductivity, [W/mK]
q'	borehole heat transfer rate per unit length, [W/m]
r	radius, [m]
t	time, [s]
u	velocity, [m/s]
x,y,z	Cartesian coordinates, [m]

Greek letters

α	thermal diffusivity, [m^2/s]
β	correlation parameter, [−]
γ	correlation parameter, [−]
ζ	integration variable, [−]
η	ground porosity, [−]
θ	relative temperature $T-T_g$, [K, °C]
κ	ground permeability, [m^2]
λ	thermal dispersivity, [m]
μ	correlation parameter, [−]
ρ	density, [kg/m^3]
φ	angle with x-axis, [rad]
χ	integration variable, [−]
ω	correlation weight, [−]

Subscripts

abs	absolute
b	borehole
H	dimensionless with reference length H
c	critical
d	Darcy
eff	effective
eq	equivalent
f	fluid
g	undisturbed ground
i,j	borehole index
k	summation index
m	mean
rb	relative to borehole radius
rel	relative
s	solid

Symbols

~	non-dimensional
*	correlated value

the design cost. Katsura et al. [11] used an experimental setup to validate the MILS theory in the case of groundwater flow. When measuring the temperature evolution at $z = H/2$ around a heat source, their results were in accordance with the theory.

A few numerical models accounting for groundwater flow are also available in literature [12-16]. Numerical models allow precise modeling by relaxing assumptions regarding ground properties, heat load profile, borehole geometry, etc. However, they require important computational resources and time, as well as a programming expertise, all of which not usually being available in most engineering projects. They are also unpractical for design optimization. To overcome this problem, a hybrid strategy using the MILS analytical model for global optimization combined with numerical modeling for post-processing was successfully applied in Ref. [17].

Although the above-mentioned literature shows that analytical models can be useful and reliable, there is still a need for more comprehensive, versatile and application-oriented tools to characterize heat transfer as a function of the many variables acting on vertical borefields in the presence of groundwater flow. In particular, such a procedure should: (i) cover all the timescales involved in geothermal applications; (ii) require no advanced programming skills or commercial software; (iii) use quantifiable and tangible variables as inputs; (iv) cover a broad range for all the variables involved. The main objective of the present paper is to develop such a procedure. The first part of the paper gives theory background and analytical solutions used for the new model. Next, we develop the combined model and we verify the precision and the limits of its applicability using finite element (FE) analysis. Finally, we present the results in the form of ground response functions (G-functions) that can be retrieved with and implemented in simple engineer-oriented procedures.

2. Description of the models used in this paper

The system under consideration is sketched in Fig. 1. It consists in a borehole of radius r_b drilled in the ground to install a vertical ground heat exchanger. Later in the paper, fields of boreholes will also be considered. In the present work, the geological environment is supposed to be such that groundwater flow is present, at a Darcy velocity u_d. Considering the ground as a saturated porous medium and assuming that groundwater flow is aligned along the x-direction, the conservation of energy equation can be written as [18]:

$$(\rho c_p)_{\text{eff}}\frac{\partial\theta}{\partial t} + (\rho c_p)_f u_d\frac{\partial\theta}{\partial x} = k_{\text{eff}}\nabla^2\theta \tag{1}$$

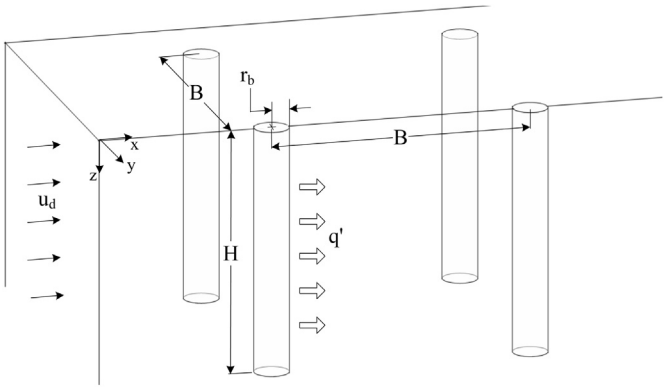

Fig. 1. Schematic representation of the ground heat exchanger system with groundwater flow.

where η is the porosity and u_d, the Darcy velocity: $u_d = \eta\, u$, and $\theta = T - T_g$ with T_g being the undisturbed ground temperature. For the sake of illustration, Table 1 presents typical values for u_d in different geological materials, assuming a hydraulic gradient of 0.01 m/m [3]. Other hydraulic and thermal properties of common soils and rocks properties can also be found in Ref. [3]. The range of possible velocities covers several orders of magnitude. This reinforces the importance of developing a design procedure taking the effect of groundwater flow into account since no "one size fits all" design is applicable to so diverse environments.

The effective values of the thermal conductivity and specific heat per unit volume also depend on the porosity of the ground matrix. For example, considering volume-averaged properties, one finds:

$$k_{\text{eff}} = \eta k_f + (1-\eta)k_s, \quad (\rho c_p)_{\text{eff}} = \eta(\rho c_p)_f + (1-\eta)(\rho c_p)_s, \quad \alpha_{\text{eff}} = k_{\text{eff}} \Big/ (\rho c_p)_{\text{eff}} \tag{2}$$

where the indices "f" and "s" refer respectively to the fluid and solid phases of the porous matrix.

When writing Eq. (1), several assumptions have been made, and it is worth to recall them in order to understand the limitations of the present work:

(i) Local thermal equilibrium is assumed, i.e. water and ground temperatures are the same;
(ii) The groundwater flow is assumed to be unidirectional and parallel to the ground surface. Furthermore, groundwater flow is supposed to be present everywhere in the ground (fully saturated soil) and to be constant in time;
(iii) All properties are assumed to be uniform and non-affected by temperature. This makes Eq. (1) linear, which is required to invoke the superposition principle;
(iv) Thermal dispersion is neglected in the present work. Thermal dispersion accounts for hydrodynamic mixing of the interstitial fluid at the pore scale [18]. Although some authors recently accounted for it in their models [19-21], few data is available for quantifying thermal dispersion of typical groundwater flows. According to Ref. [22], which presents an experimental work treating of similar ground conditions and slightly higher flow velocity conditions than those of this article, the contribution of thermal dispersion to the effective heat transfer would typically be under 5%. In a more general hydrogeological heat transfer model, one could replace the effective thermal conductivity k_{eff} of Eq. (1) by an anisotropic equivalent thermal conductivity k_{eq} taking thermal dispersion into account:

$$k_{\text{eq}} = k_{\text{eff}} + u_{\text{eff}} \begin{pmatrix} \lambda_L & 0 & 0 \\ 0 & \lambda_T & 0 \\ 0 & 0 & \lambda_T \end{pmatrix} \tag{3}$$

Table 1
Typical average groundwater Darcy velocity in various geological materials [3].

Soils	Darcy velocity[a] u_d [m/y]	Rocks	Darcy velocity[a] u_d [m/y]
Gravel	9.45×10^{2}	Karst Limestone	3.16×10^{1}
Coarse sand	2.31×10^{1}	Fractured igneous and metamorphic	4.89×10^{-1}
Fine sand	2.02	Limestone, dolomite	2.44×10^{-2}
Silt	4.47×10^{-2}	Sandstone	1.38×10^{-2}
Clay	6.86×10^{-5}	Shale	4.46×10^{-6}
		Unfractured igneous and metamorphic	7.73×10^{-7}

[a] Assuming hydraulic gradient of 0.01 m/m.

where λ_L and λ_T are the longitudinal (parallel to flow) and transverse (perpendicular to flow) dispersivity coefficients respectively. Eq. (3) is written for flows in x-direction only. In any case, including thermal dispersivity in the problem would preserve the linearity and thus, the method developed in this paper could be extended to situations where this phenomenon would be important.

Initially, the domain is entirely at $\theta = 0$. The boundary conditions that apply are: $\theta = 0$ far from the borehole (when $r \to \infty$ or $z \to \infty$), as well as at the ground surface ($z = 0$), and an imposed heat transfer rate on the surface of the borehole:

$$-k\nabla\theta|_{\text{borehole}} = \frac{q'}{2\pi r_b} \tag{4}$$

where $q' = q/H$ is the heat transfer rate per unit length, uniformly distributed over all the borehole depth H. At this point, it is assumed that the heat input q is constant. Based on the superposition principle, it is possible to model a transient heat input by combining solutions for different heat pulses, as described in ASHRAE [2].

Eq. (1) can be non-dimensionalized in the following way:

$$\frac{\partial\tilde{\theta}}{\partial \text{Fo}} + \text{Pe}\frac{\partial\tilde{\theta}}{\partial\tilde{x}} = \nabla^2\tilde{\theta} \tag{5}$$

where

$$\tilde{\theta} = \frac{\theta}{\left(\frac{q'}{2\pi k_{\text{eff}}}\right)}, \quad \tilde{x},\tilde{y},\tilde{z},\tilde{r} = \frac{\tilde{x},\tilde{y},\tilde{z},\tilde{r}}{r_b}, \quad \text{Fo} = \frac{\alpha_{\text{eff}} t}{r_b^2}, \quad \text{Pe} = \frac{u_{\text{eff}} r_b}{\alpha_{\text{eff}}}, \quad u_{\text{eff}} = \frac{(\rho c_p)_f}{(\rho c_p)_{\text{eff}}} u_d \tag{6}$$

Note that the reference length chosen in this article is the borehole radius r_b, except in Section 2.1, where it is the vertical borehole length H, for modeling purposes.

In the limit where the Peclet number vanishes, Eq. (5) becomes the conduction equation. Additionally, when considering only radial conduction, one obtains the equation that is normally used in order to size ground heat exchangers. It is commonly called the infinite cylinder source (ICS) [23]. Different solutions can be obtained from Eq. (5) depending on the limits considered (e.g., vanishing r_b, vanishing Pe, etc.) and on the solving approach (e.g., numerical versus analytical solutions). In developing the proposed heat transfer calculation procedure with groundwater flow, three models have been used: (i) Moving finite line source model (MFLS), (ii) Infinite cylindrical source (ICS), and (iii) 3D finite element model (FE). These three models are summarized in the next three subsections and are sufficient for the purpose of this paper. Note that other models are available in literature, in particular to describe short-term heat transfer mechanisms within ground heat exchangers by taking into account the non-uniformity of the heat load along the borehole or the effect of the grout [24-26]. However, these aspects are known to have virtually no effect on the medium or long-term behavior of the borehole. As will be demonstrated below, groundwater flow is more influential on medium and short-term responses of ground heat exchangers, and not so much for the short-term response. This is why in this paper only the three models mentioned above are considered. To study more comprehensively the short-term heat transfer mechanisms with groundwater advection, a more refined model including the detailed geometry and properties of the borehole would be required.

For borehole sizing purposes, one needs to calculate the borehole wall temperature evolution with time $\theta_b(\text{Fo})$. A general way to express it is through a ground function $G(\text{Fo})$, acting as a

dimensionless thermal resistance between the borehole wall and the far-off (undisturbed) ground:

$$\theta_b(\mathrm{Fo}) = \frac{G(\mathrm{Fo})}{k_{\mathrm{eff}}} q' \tag{7}$$

Using the definition for $\tilde{\theta}$ in Eq. (6), one finds that $G(\mathrm{Fo})$ is an alternative notation for $\tilde{\theta}_b(\mathrm{Fo})/2\pi$. Note that the nomenclature G used in this paper refers to ground thermal response in a general manner (i.e. it does not depend on the mathematical model used). Therefore, it does not refer specifically to the infinite cylindrical source (ICS) ground function (also noted G in literature) or Eskilson's g-functions [5].

2.1. Moving finite line source (MFLS)

The moving finite line source model (MFLS) was developed by Molina-Giraldo et al. [9] by using a methodology similar to the finite line source model [27,28], but with the application of the moving source theory [23]. It is an analytical solution to Eq. (5) that takes advantage of the fact that the problem can be seen as the one of a line source, with bore radius $r_{b,\mathrm{MFLS}} \to 0$ and with a finite length H, that would be moving in a porous media. Considering this, it is more relevant to set H as the reference length (for dimensionless expression of the variables, see Eq. (6)) instead of r_b for the analytical development of MFLS model. The solution for temperature at any point in the ground $(\tilde{r}, \varphi, \tilde{z})_H$ at any time Fo_H, and considering the flow velocity Pe_H is given by Ref. [9]:

$$\tilde{\theta}(\tilde{r}, \varphi, \tilde{z}, \mathrm{Fo}, \mathrm{Pe})_H = \exp\left[\frac{\mathrm{Pe}}{2}\tilde{r}\cos\varphi\right]\left[\int_0^1 f\left(\tilde{S}, \mathrm{Fo}, \mathrm{Pe}\right)\mathrm{d}\tilde{z}' - \int_{-1}^{0} f\left(\tilde{S}, \mathrm{Fo}, \mathrm{Pe}\right)\mathrm{d}\tilde{z}'\right] \tag{8}$$

where

$$f\left(\tilde{S}, \mathrm{Fo}, \mathrm{Pe}\right)_H = \frac{1}{4\tilde{S}}\left[\exp\left(-\frac{\mathrm{Pe}}{2}\tilde{S}\right)\mathrm{erfc}\left(\frac{\tilde{S} - \mathrm{PeFo}}{2\sqrt{\mathrm{Fo}}}\right) + \exp\left(\frac{\mathrm{Pe}}{2}\tilde{S}\right)\mathrm{erfc}\left(\frac{\tilde{S} + \mathrm{PeFo}}{2\sqrt{\mathrm{Fo}}}\right)\right] \tag{9}$$

$$\tilde{S} = \sqrt{\tilde{r}^2 + (\tilde{z} - \tilde{z}')^2}$$

where, again, the reference length for all non-dimensional parameters is H instead of r_b (see Eq. (6)).

We recall that the objective of the model is to assess the overall temperature evolution of a borehole. However, since Eq. (8) gives the temperature perturbation in a single point, one needs to integrate the equation over the entire surface of the borehole (i.e. over the whole depth $0 \le \tilde{z} \le 1$ and over the half-circumference $0 \le \varphi \le \pi$ at the effective (real) borehole radius $\tilde{r} = \tilde{r}_b$). The integrated average dimensionless temperature of the borehole is then given by:

$$\tilde{\theta}_b(\tilde{r}_b, Fo, Pe)_H = \frac{1}{\tilde{r}_b \pi}\int_0^1\left[\int_0^{\pi}\tilde{\theta}(\tilde{r}_b, \varphi, \tilde{z}, \mathrm{Fo}, \mathrm{Pe})\mathrm{d}\varphi\right]\mathrm{d}\tilde{z} \tag{10}$$

By isolating and solving the integral over φ [7], we obtain:

$$\tilde{\theta}_b(\tilde{r}_b, \mathrm{Fo}, \mathrm{Pe})_H = I_0\left(\frac{\mathrm{Pe}}{2}\tilde{r}_b\right)\int_0^1\left[\int_0^1 f\left(\tilde{S}, \mathrm{Fo}, \mathrm{Pe}\right)\mathrm{d}\tilde{z}' - \int_{-1}^{0} f\left(\tilde{S}, \mathrm{Fo}, \mathrm{Pe}\right)\mathrm{d}\tilde{z}'\right]\mathrm{d}\tilde{z} \tag{11}$$

where I_0 is the I-type Bessel function of order 0 and $f(\tilde{S}, \mathrm{Fo}, \mathrm{Pe})$ is developed in Eq. (9). One is left with a double integral that can be solved with a numerical integration algorithm. However, this is computationally expensive, especially since our interest is to develop an easy-to-use analytical model. In this paper, we thus introduce a new simplified formulation to reduce the double integral formulation of Eq. (11) into a sum of single integrals. It is inspired by the procedure used by Lamarche and Beauchamp [28] for reducing computational times associated with the finite line source model (FLS). Since the methodology is similar to that in Ref. [28] (although applied to a different mathematical function) only the result is shown here:

$$\tilde{\theta}_b(\tilde{r}_b, \mathrm{Fo}, \mathrm{Pe})_H = I_0\left(\frac{\mathrm{Pe}}{2}\tilde{r}_b\right)\left(A(\tilde{r}_b, \mathrm{Fo}, \mathrm{Pe}) + B_1(\tilde{r}_b, \mathrm{Fo}, \mathrm{Pe}) + B_2(\tilde{r}_b, \mathrm{Fo}, \mathrm{Pe})\right) \tag{12}$$

where

$$A(\tilde{r}_b, \mathrm{Fo}, \mathrm{Pe}) = \frac{1}{2}\int_{\tilde{r}_b}^{\sqrt{\tilde{r}_b^2+1}}\left(-1 + \frac{1}{\sqrt{\zeta^2 - \tilde{r}_b^2}}\right)\left[\exp\left(\frac{-\mathrm{Pe}}{2}\zeta\right)\mathrm{erfc}\left(\frac{\zeta - \mathrm{Pe\,Fo}}{2\sqrt{\mathrm{Fo}}}\right) + \exp\left(\frac{\mathrm{Pe}}{2}\zeta\right)\mathrm{erfc}\left(\frac{\zeta + \mathrm{Pe\,Fo}}{2\sqrt{\mathrm{Fo}}}\right)\right]d\zeta$$

$$B_1(\tilde{r}_b, \mathrm{Fo}, \mathrm{Pe}) = \frac{1}{4}\int_{\tilde{r}_b}^{\sqrt{\tilde{r}_b^2+4}}\exp\left(\frac{-\mathrm{Pe}}{2}\zeta\right)\mathrm{erfc}\left(\frac{\zeta - \mathrm{Pe\,Fo}}{2\sqrt{\mathrm{Fo}}}\right) + \exp\left(\frac{\mathrm{Pe}}{2}\zeta\right)\mathrm{erfc}\left(\frac{\zeta + \mathrm{Pe\,Fo}}{2\sqrt{\mathrm{Fo}}}\right)\mathrm{d}\zeta \tag{13}$$

$$B_2(\tilde{r}_b, \mathrm{Fo}, \mathrm{Pe}) = \frac{1}{2}\int_{\tilde{r}_b}^{\sqrt{\tilde{r}_b^2+4}}\left(\zeta^2 - \tilde{r}_b^2\right)^{-1/2}\left[\exp\left(\frac{-\mathrm{Pe}}{2}\zeta\right)\mathrm{erfc}\left(\frac{\zeta - \mathrm{Pe\,Fo}}{2\sqrt{\mathrm{Fo}}}\right) + \exp\left(\frac{\mathrm{Pe}}{2}\zeta\right)\mathrm{erfc}\left(\frac{\zeta + \mathrm{Pe\,Fo}}{2\sqrt{\mathrm{Fo}}}\right)\right]\mathrm{d}\zeta$$

where the reference length for non-dimensional parameters is H (replace r_b with H in Eq. (6)). The B_1 and B_2-integrals are distinguished from the A-integral because they are obtained by the method of images [5], which is used to maintain the boundary condition $\theta|_{\tilde{z}=0} = 0$. The A, B_1 and B_2 integrals can be solved by using a numerical algorithm such as the Gauss-Kronrod quadrature implemented in the Matlab function *quadgk*. The speed of calculation is around 400 times faster when solving Eq. (12) with *quadgk* instead of Eq. (11) with *dblquad* in Matlab, while yielding no discrepancy.

Eq. (12) gives the overall dimensionless temperature perturbation of a borehole due to its own heat load, corresponding to G_1 in Section 4. However, in a borefield containing many boreholes, one must compute the overall temperature rise at the borehole location using the spatial superposition principle. The addition of the effect of all the N boreholes j at a borehole i is computed as following:

$$\tilde{\theta}_i = \tilde{\theta}_b(\tilde{r}_b, \mathrm{Fo}, \mathrm{Pe})_H + \sum_{\substack{j=1 \\ i\neq j}}^{N} \left[\exp\left[\frac{\mathrm{Pe}}{2}\tilde{r}_{i,j}\cos\varphi_{i,j}\right] \left(A(\tilde{r}_{i,j}, \mathrm{Fo}, \mathrm{Pe}) + B_1(\tilde{r}_{i,j}, Fo, Pe) + B_2(\tilde{r}_{i,j}, \mathrm{Fo}, \mathrm{Pe})\right)\right] \tag{14}$$

where

$$\tilde{r}_{i,j} = \sqrt{(\tilde{x}_i - \tilde{x}_j)^2 + \left(\tilde{y}_i - \tilde{y}_j\right)^2} \quad \text{and} \quad (\tilde{r}_{i,j}\cos\varphi_{i,j}) = \tilde{x}_i - \tilde{x}_j \tag{15}$$

where the reference length for non-dimensional parameters is H (replace r_b with H in Eq. (6)). The first term of the right hand side of Eq. (14) is directly computed by Eqs. (12) and (13), and the A, B_1 and B_2 terms are also computed in the same fashion as in Eq. (13), but with a different radius.

Finally, the overall temperature perturbation over the N boreholes i is given by:

$$\bar{\tilde{\theta}} = \sum_{i=1}^{N} \tilde{\theta}_i \Big/ N \tag{16}$$

where the $\tilde{\theta}_i$ are computed with Eq. (14). Eq. (16) will be used in Section 4 for computing the transient value of the overall thermal resistance of the borefield, (G-function) also referred to as G_N.

2.2. Infinite cylindrical source (ICS)

The infinite cylindrical source (ICS) developed by Ingersoll et al. [29] has been used by many authors [30-32] as well as in the sizing procedure recommended by ASHRAE [2]. This analytical model does not take into account groundwater flow, and is thus valid when $\mathrm{Pe}\to 0$. It also neglects axial conduction (in the z-direction), which induces significant errors for long time scales. However it allows for a more representative modeling of the borehole cylindrical geometry. This makes the ICS model generally more precise than line source-type models for short time scales, when most of the temperature perturbation is located near the borehole [33]. The temperature perturbation at a distance $\tilde{r} = r/r_b$ from the borehole center is given by:

$$\tilde{\theta}(\tilde{r}, \mathrm{Fo})_{r_b} = \frac{2}{\pi}\int_0^{\infty} \left[\left(\frac{e^{-\chi^2 \mathrm{Fo}} - 1}{J_1^2(\chi) + Y_1^2(\chi)}\right)\left(\frac{J_0(\tilde{r}\chi)Y_1(\chi) - J_1(\chi)Y_0(\tilde{r}\chi)}{\chi^2}\right)\right] \mathrm{d}\chi \tag{17}$$

where the reference length for non-dimensional parameters is r_b (see Eq. (6)). The temperature perturbation at borehole radius $\tilde{\theta}(\tilde{r}_b = 1)$ will be used in Section 4 for computing the transient value of the G-function G_1 giving the ground thermal resistance of a single borehole. We could add the effect of the other surrounding boreholes by summation, as we did for MFLS model in Eqs. (14)–(16) to obtain the overall G-function of a borefield G_N. However, we will see in Section 3 that ICS should only be used for short time scales over which no interaction between boreholes is typically reached (with reasonable borehole spacing).

2.3. 3D finite element model (FE)

Finally, it is also possible to model the domain of Fig. 1 with finite elements (FE) or finite volumes, and to solve directly Eq. (5) within the domain. Here, a commercial finite element software was used [34]. Quadratic elements were chosen to discretize the domain of Fig. 1. Cases with a single borehole and with a 16-borehole field were tested. In every case, only the ground around the boreholes was modeled (i.e., boreholes are cylindrical holes in the domain).

The undisturbed ground temperature in the entire domain is set as the initial condition of the time dependent problem. The boundary conditions are the following. A uniform and constant heat flux is imposed through the cylindrical boundaries representing the boreholes. Considering that the groundwater flows in the x-direction, a symmetry plane x-z is used to halve the size of the domain. At the ground surface, the undisturbed ground temperature is imposed. Finally, at the other boundaries, an infinite element zone is added. Although a no-flux condition is applied by default, it was verified that the boundary condition of the infinite zones have no effect on the simulation results. A uniform velocity field is applied throughout the domain, including in the infinite zones. After the simulations, the average temperature on the borehole wall(s) is extracted from the temperature data to compute the value of the G-function, using Eq. (7).

The mesh independence was considered to be reached when doubling the number of elements of the domain yielded a relative discrepancy of less than 1% on the borehole surface temperature for every time-step in the considered range. As an example, the final mesh contained around 4700 elements for the case of a single borehole and 36,800 elements for the 16-borehole field. An adaptive time-stepping algorithm, the backward differentiation formula (BDF), already implemented in the software, was used. The time-stepping independence was reached by successively refining the time-stepping tolerance by one order of magnitude until it yielded a relative discrepancy of less than 0.01% on the average borehole surface temperature for every time-step in the considered range.

The FE model was validated with the analytical MFLS (§2.1) and ICS (§2.2) models by doing a series of different simulations. For each case, the simulation parameters, geometries and boundary conditions were set in such a way that the assumptions relative to the analytical models were met. Less than 1% of discrepancy was obtained for every case on the G-function for the entire time-range considered. Therefore, the FE model was considered to be validated.

3. Precision of the analytical models as a function of timescale

Before developing the heat transfer calculation procedure to take into account groundwater flow, it is worth to describe briefly the precision and range of validity of the three models described above. The FE model is considered as the more precise model in the sense that it does not involve any specific assumption in terms of $\tilde{H}$, or Pe. It also allows for much more freedom regarding boundary

conditions, non-homogeneity of the domain, temperature-dependent properties, etc. However, its disadvantage is that solving such a model is time consuming. For example, for simulating a 64 borehole fields over a 10 year period, the FE model would require a few hours of simulations compared to few seconds for the analytical models (MFLS or ICS), which makes the FE model impractical for engineering design purpose. If the G-function is only required for a few specific times (such as in the heat pulse design method used by ASHRAE [2]), the simulation time reduces to a few milliseconds for the analytical models, while remaining the same for FE model. Furthermore, in the case of a detailed fluctuating heat load to the borehole (not covered in this article), load aggregation algorithms [35–37] or fast Fourier transform (FFT) algorithms [38] allow using the analytical models with equivalent precision and faster than the FE models. The results shown in this section are thus not restricted to the heat pulse design methods but could also be used in more comprehensive design methods (e.g. in borehole exchanger softwares). On the other hand, despite their relative flexibility and their speed of calculation, the two analytical models both involve important simplifications. Therefore, for engineering practice, one needs to know to what extent their precision is satisfactory.

In this section, we first simulated heat injection in the ground by a single borehole with the FE model for various values of Pe and $\tilde{H}$ shown in Table 2. The non-dimensional duration (Fo) of the period simulated is also provided in Table 2. Then, we simulated the same heat injection rate with the MFLS model and with the ICS model. The results achieved with the FE model were considered as the reference, since they are presumably more realistic. The error E on average borehole wall temperature (G-function) between the MFLS and FE models was calculated as a function of Fo (i.e. time), for every combination of the parameters Pe (i.e. groundwater flow velocity) and $\tilde{H}$ in Table 2. Error was calculated as follows:

$$E_{\mathrm{MFLS}}(\mathrm{Fo}) = G_{\mathrm{MFLS}}(\mathrm{Fo}) - G_{\mathrm{FE}}(\mathrm{Fo}) \tag{18}$$

The definition of the G-functions is given in Eq. (7). We recall that the G-functions are dimensionless, so the error in Eq. (18) has no unit. The error between the ICS and FE models was also calculated in the same fashion. An example of the MFLS and ICS error curves obtained for $\tilde{H} = 2000$ and $Pe = 10^{-1.5}$ is reported in Fig. 2a. Note that the absolute value of the error $|E|$ is displayed on the vertical axis, instead of the error E, but the sign of the error is shown in the legend.

Although only one combination of parameters $\tilde{H}$ and Pe is reported in Fig. 2a, all the cases yielded similar error patterns. It is interesting to note that, in the range of Peclet numbers and $\tilde{H}$ values investigated, the ICS model (which does not consider groundwater flow) reproduces better the results of the finite element model than the MFLS for shorter times. It should be repeated here, though, that the ICS and the current FE models are not necessarily precise to describe short-term heat transfer mechanisms, and that other more comprehensive models could be used if required [24]. However, MFLS represents better the long-term heat transfer behavior of the system, while the ICS yields a G-function growing to infinity. The times at which both models are equally precise (referred to as the critical Fo, i.e. Fo_c) is indicated by a small circle in Fig. 2a. This gives the most appropriate time to switch from the ICS (or any other more comprehensive short-term model) to the MFLS model.

Table 2
Values of the variables tested for timescale analysis.

Variable	Values tested
Fo	10^{-2} to 10^{6} by $\log_{10}$ increments of 0.1
Pe	0; 10^{-3} to 10^{0} by $\log_{10}$ increments of 0.5
$\tilde{H}$	500 to 2500 by increments of 500

Although one could have expected Fo_c to be highly dependent on Pe and $\tilde{H}$, the results actually show a weak dependency on Pe, and almost no dependency on $\tilde{H}$. Fig. 2b gives the different values of Fo_c obtained in the range of Pe investigated, regardless of $\tilde{H}$.

Another important data that should be analyzed is the maximal error on the G-function that occurs during the simulated period by using an analytical model instead of a FE model. In Fig. 2c, it can be seen that the absolute value of the maximum error on the G-function, $|E_{\max}|$ (solid fitting curve, left vertical axis), is kept under 0.01 for $\mathrm{Pe} \leq 10^{-1}$. This corresponds to a relative error $|E_{\max,\mathrm{rel}}|$ (dashed curve, right vertical axis) of less than 3%. However, the error increases abruptly for higher Pe values. This means that, even by using MFLS, one cannot accurately simulate heat transfer at high Peclet numbers. This is due to the fact that in the MFLS, heat is generated by a line and not a cylinder. Indeed, using a line heat source instead of a cylinder in the FE model (see §2.3) yielded identical results as MFLS for all Pe values, including $\mathrm{Pe} > 10^{-1}$. Even if the effects of this modeling difference normally decrease when time increases, things are different when taking groundwater flow into account. In the FE model (which represents better reality), groundwater cannot flow through the grouted cylindrical boreholes, contrarily to the MFLS model, where groundwater flows everywhere in the ground. At very high Pe, this appears to cause significant errors in the G-function (MFLS under-predicting the temperature perturbation). It is thus appropriate to stay under this critical Pe number, Pe_c, when using the MFLS model. For keeping error on the G-function under 3%, the critical Pe number scales as: $Pe_c \approx 1 \times 10^{-1}$. For a typical ground subject to groundwater flow ($\alpha_{\mathrm{eff}} = 0.05\ \mathrm{m}^2/\mathrm{day}$), borehole radius ($r_b = 0.05$ m), porosity ($\eta = 20\%$) and volumetric heat capacity ratio $(\rho c_p)_f/(\rho c_p)_{eff} = 2$, this corresponds to a groundwater Darcy velocity of $u_d = 18.25$ m/year. Typically, such a flow velocity would allow reaching heat transfer steady-state in approximately one year, which is very fast for geothermal applications. Indeed, at this point, the effects of annual thermal load imbalance are somehow reset each year and we observe no long-term degradation of the performances. Now, taking a second look at Fig. 2b considering this critical Pe number $\mathrm{Pe}_c = 1 \times 10^{-1}$, one can conclude that, over the range $0 \leq \mathrm{Pe} \leq \mathrm{Pe}_c$, the critical Fourier number Fo_c for shifting from ICS to MFLS, can be approximated as a constant $\mathrm{Fo}_c \approx 20$.

The main conclusions of the time-validity analysis of this section are the following. (i) For short-term thermal aspects (i.e. for times smaller than the critical time Fo_c) radial conduction dominates and ICS can be qualified of adequate (but more comprehensive models without groundwater flow are available as well and could be considered), and for long-term (i.e. for times larger than Fo_c), groundwater flow and axial conduction become more important and should be taken into account by using the MFLS model; (ii) However, undesirable groundwater advection effects "inside the borehole" prevent from using MFLS at high Pe. The modeling approach presented in this article is thus valid with Pe numbers under $\mathrm{Pe}_c = 1 \times 10^{-1}$. With such a strategy, the error on the G-functions generated by the analytical solutions due to their limitations is always smaller than 3%, which corresponds to an absolute error of 0.01 for all Fourier and Peclet numbers considered as shown in Fig. 2c. In all cases, it was verified that the ratio $\tilde{H} = H/r_b$ had no significant influence on the precision of the models.

4. Presentation of new G-functions

This section presents the ground functions obtained for the various design and operating parameters considered so far. All results reported in the present section were computed with a *Matlab* code in which the analytical models described in Section 2 have

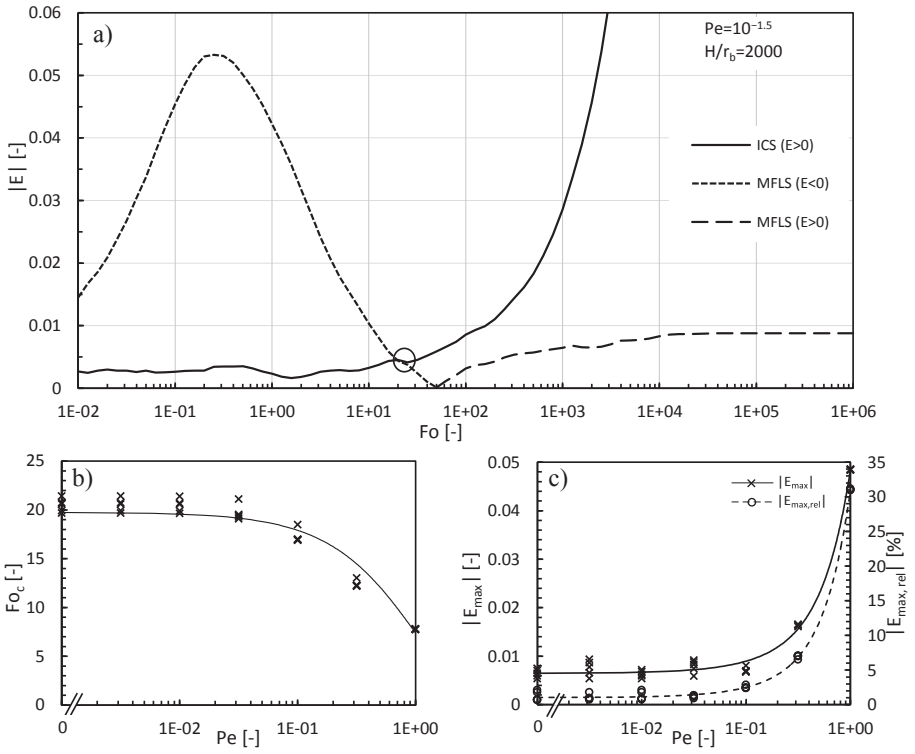

Fig. 2. a) Error curves for MFLS and ICS model, based on Eq. (18) b) Critical Fo number, Fo_c, as a function of Pe c) Maximum error induced by using analytical model as a function of Pe.

been implemented. Although such a code can directly provide precise values of the ground function, and could thus be used by borehole designers, its implementation can be quite tedious. This section thus aims at providing other practical tools for evaluating ground functions in the context of a more engineering-oriented ground heat exchanger sizing procedure.

4.1. Single borehole

This section provides a graphical tool for evaluating the G-function of a single borehole, here denoted G_1. It can be expressed as a function of three variables: time, groundwater flow velocity, and borehole depth. These quantities are recast in dimensionless form, as shown in Eq. (6): $\mathrm{Fo} = \alpha_{\mathrm{eff}} t / r_b^2$, $\mathrm{Pe} = r_b u_{\mathrm{eff}} / \alpha_{\mathrm{eff}}$, and $\tilde{H} = H / r_b$. In Section 4, the reference length will always be the borehole radius r_b (not the vertical length H). As mentioned in Section 3, the ICS (see Eq. (17)) and MFLS (see Eq. (12)) models are used to compute G_1. Note that Eq. (12) is presented with H as the reference length for dimensionless parameters, so Fo and Pe were simply converted adequately to $\mathrm{Fo_H}$ and $\mathrm{Pe_H}$ before solving, and reconverted afterwards. Fig. 3 shows $G_1(\mathrm{Fo})$ obtained with the ICS model as well as with the MFLS model considering various Pe and $\tilde{H}$ values. In Fig. 3a, the case $\tilde{H} = 1500$ is shown for all the time range considered $10^{-2} \leq \mathrm{Fo} \leq 10^6$. The parts of the curves that should not be used according to the time scale analysis of Section 3 have been dashed. $G_1(\mathrm{Fo} \geq 10^2)$ is given for other values of $\tilde{H}$ in Fig. 3b to e. For $\mathrm{Fo} \leq 10^2$, $\tilde{H}$ and Pe have virtually no influence on G_1 (axial conduction and radial advection in the ground are negligible).

For the segment dominated by groundwater flow and/or axial conduction (i.e. for Fo above $\mathrm{Fo_c}$), a steady-state in which temperature does not change is eventually reached. The steady-state is reached faster when Pe is large. Also, it is visible from Fig. 3 that the presence of groundwater can significantly facilitate the heat transfer from the borehole. Thermal effects of the groundwater flow on the borehole become apparent when Pe is above ~10^{-4}. Another interesting fact is that the influence of $\tilde{H}$ decreases when Pe increases. In other words, at high Pe number, groundwater advection effects take over axial conduction effects.

For its implementation within a spreadsheet, it is more convenient to express $G_1(\mathrm{Fo}, \mathrm{Pe}, H/r_b)$ with a correlation. In order to capture the proper behavior of the function, a correlation has been developed, combining two functions with asymptotic behaviors:

$$G_{1,Y}^*(\chi) = Y_1 + \sqrt{Y_2\chi^2 + Y_3\chi + Y_4} + \frac{Y_5}{\sqrt{Y_6\chi - Y_7}} \tag{19}$$

$$G_{1,Z}^*(\chi) = \frac{Z_1(\chi - \varepsilon)^3}{(\chi - \varepsilon)^2 + 20^{-(\chi - \varepsilon - Z_2)/Z_3} + Z_4} \tag{20}$$

$$\chi \equiv \log_{10}(\mathrm{Fo})$$

and G_1^* is obtained with:

$$G_1^* = G_{1,Y}^* - G_{1,Z}^* \tag{21}$$

The asterisk denotes a correlated value (versus an analytically computed value). Y_{1-7} and Z_{1-4} are empirical coefficients that have been determined by minimizing the error between the correlation and the actual value of G_1. Their values are constant (i.e. completely independent of Fo, Pe, etc.) and given in Table 3. The coefficient ε in Eq. (20) can be computed with a summation of 10 terms depending of Pe and $\tilde{H}$:

$$\varepsilon = \sum_{k=1}^{10} \omega_{G_{1,k}} V_{G_{1,k}} \tag{22}$$

where $\omega_{G_{1,k}}$ is the weight associated with variable combination k and $V_{G_{1,k}}$ is the kth variable combination. The $\omega_{G_{1,k}}$ and $V_{G_{1,k}}$ are shown in Table A1, in appendix.

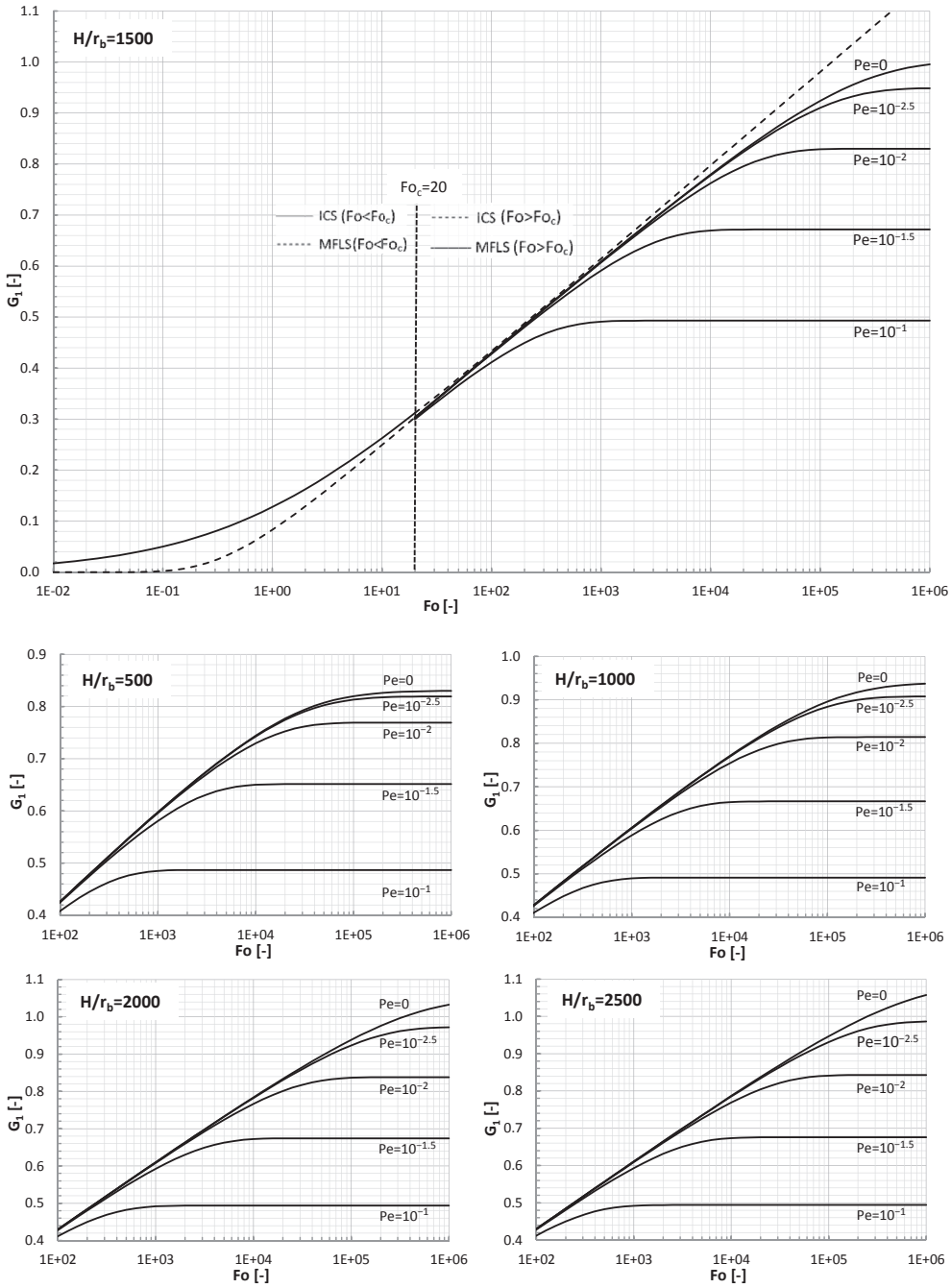

Fig. 3. Ground function for a single borehole G_1, as a function of Fo, Pe and $\tilde{H}$

Due to space limitation, it is not possible to present a figure comparing the correlation versus the actual values of G_1. Based on a test with 500 randomly generated sets of variables in the range $10^{-4} \leq \mathrm{Pe} \leq 10^{-1}$ and $500 \leq \tilde{H} \leq 2500$, each evaluated at 20 Fo-values between 10^{-2} and 10^{8}, the maximum absolute error on the ground function was 0.0366, which shows the high level of precision of the correlation.

4.2. Multiple boreholes

With geothermal fields containing more than one borehole, thermal interactions may occur between them after a certain time, enhancing the total effective ground thermal resistance. This translates into a general temperature rise at the borehole walls, referred to as a penalty temperature (T_p), a concept that is used, among others, in the design procedure of ASHRAE [2]. This penalty temperature can be expressed in a non-dimensional form by a G-function solely due to borehole interactions, here noted G_{N1}. The

Table 3
Coefficients Y and Z for Eqs. (7) and (8).

k	Y_k	Z_k
1	2.1593E+00	1.5325E−01
2	1.5080E−02	5.3963E+00
3	5.8176E−03	1.9551E+00
4	3.7124E−02	2.5489E+01
5	−9.7071E+00	
6	1.5830E+00	
7	−1.9030E+01	

present study will focus on ground thermal response functions, because they offer more versatility than T_p: they can show time-evolution of the borehole interactions, not only their effect after 10 years. Furthermore, they do not depend on heat load or ground thermal conductivity. Note that T_p can be retrieved from the ground functions if desired. More information about the interpretation and computation methods of T_p is available in Refs. [39,40]. The increase of the G-function due to borehole interactions G_{N1} is computed as the difference between the overall G-function for the N boreholes G_N and the G-function for a single borehole G_1 [41]:

$$G_{N1} = G_N - G_1 \tag{23}$$

In this section G_{N1} is directly computed from the *Matlab* implementation of Eqs. (16) and (12) for G_N and G_1 respectively, shown in Section 2.

We assume that the borefield pattern is rectangular with the boreholes aligned and evenly spaced. We also assume the exchanger's length to be the same for each borehole. When considering unidirectional groundwater advection, G_N and G_{N1} are thus functions of seven dimensionless variables: the Fourier number (time) Fo, the number of boreholes N, the aspect ratio (longest side/shortest side) of the borefield A, the pitch angle (orientation) between the borefield longest side axis and the flow φ, the borehole separation distance $\tilde{B} = B/r_b$, the borehole vertical length $\tilde{H} = H/r_b$, and the Peclet number (groundwater flow velocity) Pe. The simulated range for each variable is shown in Table 4.

We recall that the goal of this sub-section is to provide a practical tool for evaluating G_{N1} for any combination of the variables in typical operating conditions. However, with seven variables and important levels of interaction (cross-effects) between them, simple graphical representation of G_{N1} like for G_1 is not possible. Even tables with a few sets of computed values for specific cases would be far from covering the complete possibilities of scenarios. Finally, a unique correlation expressing G_{N1} as a function of a weighted sum of different variable combinations was tried but did not yield satisfactory results. Bernier et al. [41] used such a methodology for presenting temperature penalty results for geothermal borefields without groundwater flow. However, it was a 4-variable problem, and they needed a 36-term (36 variable combinations) correlation to achieve satisfying results. In our case, groundwater flow brings three more variables into the problem, which increases considerably the complexity of such a task.

The fitting procedure is thus carried on in two steps: (i) A general parametric curve is drawn for G_{N1}(Fo) as a function of time only (Section 4.2.1), and (ii) Then, correlations are found to express the parameters of that curve, as a function of the six remaining variables (Section 4.2.2). The step-by-step procedure for computing G_{N1} is described schematically in Fig. 4.

4.2.1. Time-dependent parametric curve fitting G_{N1}(Fo)

When analyzing G_{N1} results for any combination of the problem variables, we observe a typical behavior regarding its evolution with time, i.e. G_{N1} vs Fo. This behavior can be fitted with an analytical expression containing 3 parameters:

$$G_{N1}(Fo) \approx \gamma\left[1 - \frac{1}{e^{(\log_{10}(Fo)-\mu)/\beta}+1}\right] \tag{24}$$

where γ, β, and μ are the three parameters to fit. The last term in the bracket is the Fermi function [42]. Fig. 5 shows the general time-dependent parametric curve (in solid line) and the graphical interpretation of its parameters. In our case, the parameter γ represents the steady-state value of G_{N1} ($G_{N1,ss}$), μ is the logarithm of the time at which $G_{N1} = 0.5\, G_{N1,ss}$, and β is the log-scale time span between $G_{N1} = G_{N1,ss}/(e+1) \approx 0.27 G_{N1,ss}$ and $0.5 G_{N1,ss}$. However, instead of forcing the fit at 27% and 50% of the steady-state value, some tests revealed that the overall function fit is generally improved when forcing the correspondence at 10% and 90% of the steady-state value. By analytic treatment of Eq. (24), the parameters are thus recalculated in the following way:

$$\gamma \to G_{ss},\ \mu \to \left(Fo_{90\%}^{\log} + Fo_{10\%}^{\log}\right)/2,\ \beta \to \left(Fo_{90\%}^{\log} - Fo_{10\%}^{\log}\right)/4.4 \tag{25}$$

where

$$Fo_{10\%}^{\log} \equiv \log_{10}\left(Fo|_{G_{N1}=0.1G_{N1ss}}\right) \quad \text{and} \quad Fo_{90\%}^{\log} \equiv \log_{10}\left(Fo|_{G_{N1}=0.9G_{N1ss}}\right) \tag{26}$$

Note that G_{ss} is used as a lighter notation for $G_{N1,ss}$. In Fig. 5, a typical fitted $G_{N1}(\log_{10}(Fo))$ curve is also shown in dashed line, to illustrate the similarity with the Fermi function. Such curves were plotted for various combinations of variables to ensure the applicability of this fitting curve over the whole range considered (see Table 4). In these cases, the fitting parameters γ, β, and μ were extracted directly from the results of G_{N1} computed with the *Matlab* procedure implemented. They were considered to be "exact values" and thus represent a "best case" fit. However, for practical purposes explained before, empirical expressions for γ, β, and μ must be found. This will be done in the next sub-section.

4.2.2. Empirical estimation of the fitting parameters

The goal of this section is to present empirical expressions to describe the influence of the six remaining variables (N, A, φ, $\tilde{B}$, $\tilde{H}$, Pe) on the fitting parameters G_{ss}, $Fo_{10\%}^{\log}$ and $Fo_{90\%}^{\log}$ (which yield γ, β, and μ, see Eq. (25)), needed in Section 4.2.1.

Table 4
Simulated range for all variables.

Variable	Values tested
Fo	10^{-2} to 10^{8}
N	2 to 81 (up to 9 on each side)
A	1 to 9
φ	0 to π/2
$\tilde{B}$	50 to 200
$\tilde{H}$	500 to 2500
Pe	10^{-4} to 10^{-1}

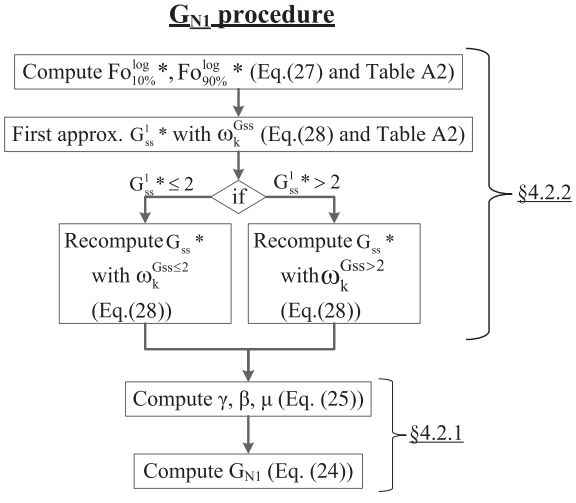

Fig. 4. Schematic procedure for evaluating G_{N1}.

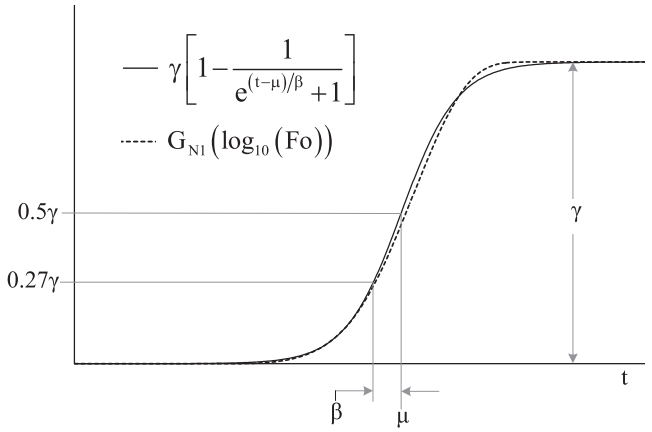

Fig. 5. General time-dependent parametric fitting curve for G_{N1}(Fo).

A total of 2000 scenarios were generated randomly. The possible range for each of the six variables (N, A, φ, $\tilde{B}$, $\tilde{H}$, Pe) is shown in Table 4 above. Each scenario was solved for G_{N1} over the whole time range considered: Fo = 10^{-2} to 10^{8}, in such a way that the reference ("real") parameters G_{ss}, $Fo^{log}_{10\%}$ and $Fo^{log}_{90\%}$ could be extracted from the results. Note that the time range was extended to Fo = 10^{8} (contrarily to 10^{6} in Section 4.1) to ensure that at least 90% of the steady-state is reached and that $Fo^{log}_{90\%}$ can be found in every case.

As mentioned earlier, the high number of remaining variables (i.e., 6), plus the high level of cross-effects between them, makes it difficult to reach accurate correlations with simple expressions. Satisfying fits were obtained for the parameters $Fo^{log}_{10\%}$ and $Fo^{log}_{90\%}$ by using a weighted sum of 64 terms that are combinations of the six variables. Based on a sensitivity analysis, is was attempted to eliminate less influential terms, but the level of precision was not as good, and therefore, the 64 terms were kept to develop the correlations. For example, the fitted parameter $Fo^{log}_{10\%}$ (noted $Fo^{log}_{10\%}*$) is computed by:

$$Fo^{log}_{10\%}* = \sum_{k=1}^{64} \omega_k^{Fo^{log}_{10\%}} V_k \tag{27}$$

where $\omega_k^{Fo^{log}_{10\%}}$ is the weight associated with variable combination k for the parameter $Fo^{log}_{10\%}$, and V_k is the kth variable combination. The ω_k and V_k are shown in Table A2, in appendix. The weights for each coefficient were computed with *lsqlin*, a linear least-square minimization algorithm, already implemented in *Matlab*.

However, although the correlations for $Fo^{log}_{10\%}$ and $Fo^{log}_{90\%}$ were satisfactory, the 64-term correlation for the parameter G_{ss} was found to be imprecise, with a coefficient of determination $R^2 = 0.9421$, a maximum absolute error $E_{abs,\,max} = 3.41$, and more than 10% of the data falling in the range $G_{ss} < 0$, which is not physically plausible. To improve the fitting, it was then decided to split the distribution in two parts ($G_{ss} \leq 2$ and $G_{ss} > 2$) and compute a separate set of ω_k for each part. In order to compute G_{ss}, one should thus calculate a first approximation $G^1_{ss}*$ and then choose between the weight sets $\omega_k^{Gss\leq 2}$ and $\omega_k^{Gss>2}$ for a second (more precise) computation $G^2_{ss}*$:

$$G^1_{ss}* = \sum_{k=1}^{64} \omega_k^{Gss} V_k, \text{then} \begin{cases} G^2_{ss}* = \sum_{k=1}^{64} \omega_k^{Gss\leq 2} V_k & \text{if} G^1_{ss}* \leq 2 \\ G^2_{ss}* = \sum_{k=1}^{64} \omega_k^{Gss>2} V_k & \text{if} G^1_{ss}* > 2 \end{cases} \tag{28}$$

The ω_k and V_k required are shown in Appendix A2. This second iteration allows to reach a satisfactory fit. Note that using different sets of ω_k for the same parameter causes a discontinuity hypersurface in the fitted function G_{ss}* (N, A, φ, $\tilde{B}$, $\tilde{H}$, Pe). However, since the function does not have to be differentiated, this does not affect the methodology. In a few rare cases, it may happen that, for example, $G^2_{ss}* > 2$ even if $G^1_{ss}* \leq 2$. Then, a third iteration would be needed, using $\omega_k^{Gss>2}$ for the computation of $G^3_{ss}*$. However, this case is quite unlikely to happen and is thus not shown in the schematic procedure of Fig. 4.

4.2.3. Overall fitting for G_{N1} with combined procedure

In order to verify the accuracy of the fittings described in Sections 4.2.1 and 4.2.2, 796 new random scenarios were generated (combinations of the variables N, A, φ, $\tilde{B}$, $\tilde{H}$, Pe), and for each of them, we computed G_{N1} at 10 random values of Fo (with log-scale uniform probability distribution). The Fo values were different for each scenario. The range considered for all the variables is given in Table 4. We first computed the exact value of G_{N1} for each scenario at each Fo with the *Matlab* procedure introduced earlier. Then, we used the techniques of Sections 4.2.1 and 4.2.2 to obtain an estimated value G_{N1}* based on the correlations for each scenario, at each Fo number. Fig. 6 compares the exact results (horizontal axis) against the correlated results (vertical axis), including intermediate steps required by the methodology. Coefficient of determination R^2 and maximum error E (absolute or relative) are given for every fit. Fig. 6a–c shows the fitting results of $Fo^{log}_{10\%}$, $Fo^{log}_{90\%}$, and G_{ss} respectively, for the 796 scenarios. Note that $Fo^{log}_{10\%}$, $Fo^{log}_{90\%}$, and G_{ss} depend only on the design parameters and groundwater flow properties, and not on time. Fig. 6d shows the G_{N1} result for the 796 scenarios at the 10 Fo values (7960 points). The fittings are all satisfactory, with strong coefficients of determination and low maximum error. In Fig. 6 c and d, the absolute maximum error on G is provided instead of relative error, because some cases yield $G \to 0$ and thus $E_{rel,max} \to \infty$. The correlation was also tested for the $2^6 = 64$ extreme cases corresponding to the different possible combinations of the extreme values of the variables. The correlation was found to yield errors similar to those of Fig. 6, except when the Pe value was very low (Pe = 10^{-4}). For conduction dominated scenarios, it is thus advised to rely on other existing correlations developed without groundwater flow. Otherwise (e.g., Pe $\geq 10^{-3}$), the present correlation was found to be quite robust.

5. Conclusions

This paper introduced a new set of G-functions for modeling heat transfer in geothermal borefields in the presence of groundwater flow. Infinite cylinder source (ICS) and moving line source (MFLS) models are used to generate the G-functions. A new mathematical formulation for MFLS is proposed to reduce its computational burden. The method reduces the double integral formulation into a sum of single integrals, for a computation ~400 times faster.

The validity of the ICS and MFLS analytical models was investigated as a function of the timescale considered. This was made by comparing analytical results to those of a finite element model. The results showed that even for significant flow velocity, ICS is more precise than MFLS for short timescale. Then, effects of axial conduction and heat advection (due to groundwater flow) become more important and MFLS is required. The critical Fo number (ideal time for switching from ICS to MFLS) was

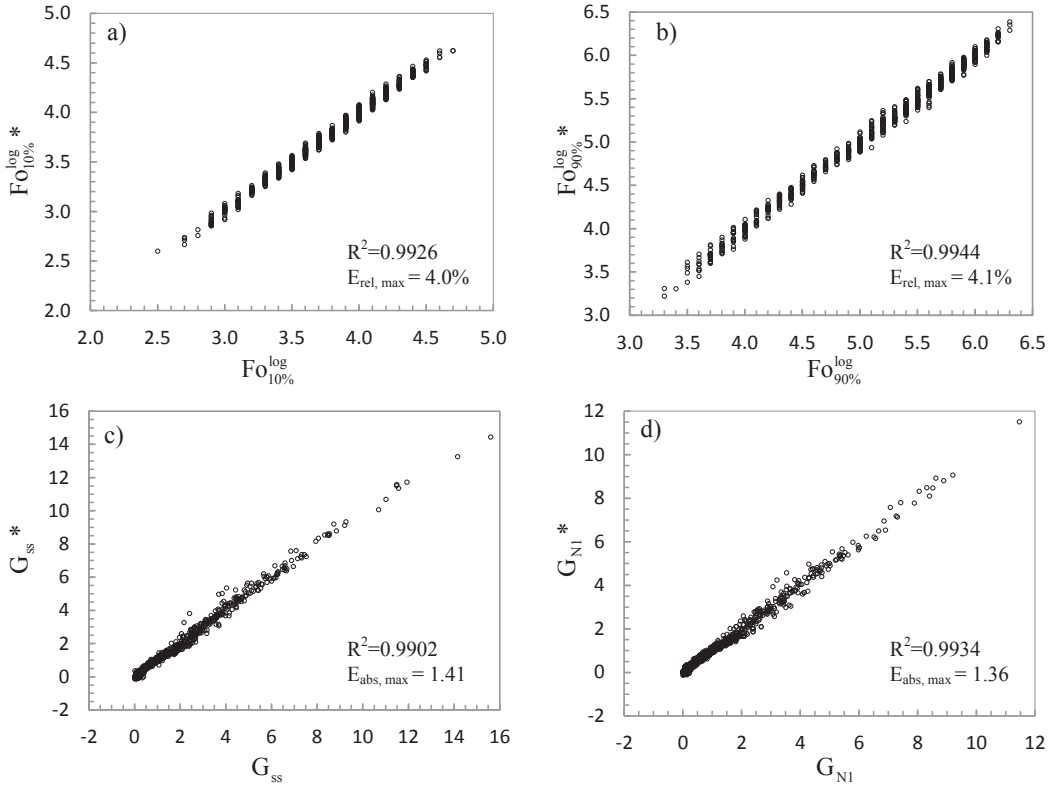

Fig. 6. Fitting results for parameters a)$Fo^{log}_{10\%}$, b)$Fo^{log}_{90\%}$, c) G_{ss} and d) final fit for G_{N1}.

established at $Fo_c \approx 20$ for the whole range of borehole vertical length and groundwater flow velocity covered in this article. As mentioned previously, it could be advisable to use more comprehensive models instead of ICS for short times (i.e. smaller than Fo_c) to account for short-term effects that can prove important in some cases [24].

In the scope of future integration to engineer-oriented design procedures, the G-functions had to be expressed in a convenient way. The borehole self-contribution to ground resistance G_1 was expressed graphically, as a function of time, flow velocity and borehole vertical length. As for the contribution of borehole thermal interactions G_{N1}, it depends on time, flow velocity and direction, number of boreholes, aspect ratio of the borefield, borehole spacing and vertical length of the borehole. The dependency to so many variables could not be expressed graphically. Instead, a combined method using curve fitting with correlated parameters was used, with determination coefficients of 0.9934 over the prescribed variable range.

Although the proposed procedure considers the effect of numerous parameters, it still relies on a series of assumptions that could be relaxed in future work, such as uniform ground and groundwater properties, no thermal dispersion, local thermal equilibrium, etc. Among these considerations, the case where groundwater flow occupies only a small layer in the ground is of great interest [14].

The new G-functions should also be validated against experimental results. Furthermore, two related topics of research are of particular interest for providing more knowledge and tools related to ground heat exchangers with groundwater flows: (i) The determination of ground and groundwater properties (e.g., thermal conductivity, hydraulic conductivity, flow direction, etc.) is a challenge, in particular due to constraints of time and cost. Methods should be developed to estimate these properties in the context of geothermal applications. Tools, methods, maps and geo-referenced database developed by hydrogeologists could be adapted to that purpose [43–44]; (ii) Design optimization in the presence of groundwater should be thoroughly investigated, for example, from a technoeconomic point of view [45]. In the end, good design practices should be established more clearly and adapted to groundwater flow.

Acknowledgments

This work was financially supported by the Fonds de recherche du Québec – Nature et Technologie (FRQNT).

Appendix A1

Table A1
Correlation variables and coefficients for computing G_1.

k	$V_{G_{1k}}$	$\omega_{G_{1k}}$
1	$\log_{10}(Pe)$	−3.1343E+00
2	H/r_b	−1.5102E−04
3	H/r_b^2	−3.6344E−07
4	H/r_b^3	8.7637E−11
5	$\log_{10}(Pe)^2$	−6.7567E−01
6	$\log_{10}(Pe)^3$	−2.7250E−02
7	$\log_{10}(Pe)\ H/r_b$	−7.6832E−04
8	$\log_{10}(Pe)\ H/r_b^2$	8.8014E−08
9	$\log_{10}(Pe)^2\ H/r_b$	−3.9060E−05
10	1	−2.4358E+00

Table A2
Correlation variables and coefficients.

k	V_k	ω_k				
		$Fo_{10\%}^{log}$	$Fo_{90\%}^{log}$	G_{ss}	$G_{ss} \leq 2$	$G_{ss} > 2$
1	B	1.6913E−02	1.3019E−02	1.2633E−01	1.4475E−02	1.0421E−01
2	$\log_{10}(Pe)$	−7.6582E−01	−1.2224E+00	7.4329E+00	3.2682E+00	4.7796E+00
3	H	−4.4557E−04	−1.2806E−04	−9.3911E−04	−2.1554E−03	−5.9186E−03
4	$\sqrt{N}$	1.0909E−01	1.9980E−01	9.2965E−02	−9.1094E−01	5.2426E−01
5	A	4.7451E−02	2.6141E−02	2.9561E−01	7.4018E−03	−2.6049E−01
6	φ	2.2358E−02	−1.3712E−01	3.8359E+00	6.8006E−01	5.3609E+00
7	φ^2	−7.6496E−02	−1.6397E−01	−1.6641E+00	−3.2538E−01	−2.2905E+00
8	φ^3	3.1136E−02	4.5295E−02	−8.9172E−02	1.1126E−01	6.1315E−02
9	A^2	−2.9758E−03	−1.2658E−03	1.1825E−02	7.5165E−03	−3.9530E−03
10	A^3	1.9855E−04	1.8749E−04	−6.3329E−04	1.0459E−04	2.7720E−04
11	A φ	−2.4589E−02	−3.9295E−02	−1.3766E−01	−6.4086E−02	−2.0302E−01
12	A φ^2	2.9996E−03	3.9504E−03	8.6379E−02	4.1964E−03	8.4937E−03
13	A^2 φ	1.2475E−03	1.9378E−03	−5.3303E−04	4.0155E−03	3.1179E−02
14	N	−1.8194E−02	−9.8506E−03	−1.6859E−02	6.5508E−02	−1.9149E−01
15	$N^{3/2}$	7.6999E−04	3.2836E−04	−1.8785E−03	−9.7776E−04	4.4431E−03
16	$\sqrt{N}\varphi$	−1.7394E−02	−3.0166E−02	−3.9147E−01	−1.3891E−01	−4.6364E−01
17	$\sqrt{N}\varphi^2$	−1.1756E−03	4.6290E−04	1.9060E−01	2.1463E−02	1.5584E−01
18	N φ	1.5200E−03	2.2891E−03	1.0117E−02	7.2408E−03	1.7477E−02
19	$\sqrt{N}$ A	−1.7712E−02	4.9786E−03	3.1110E−02	3.4845E−02	3.2091E−01
20	$\sqrt{N}$ A^2	−2.0339E−04	−9.3794E−04	−9.3580E−03	−3.6201E−03	−1.7196E−02
21	N A	1.7292E−03	−5.1660E−04	−4.6379E−04	−1.4828E−03	−3.4653E−02
22	H^2	−8.0638E−09	−8.6662E−08	−2.8482E−07	2.0418E−07	−1.5571E−06
23	H^3	2.4734E−11	3.5192E−11	1.1477E−10	8.7791E−11	4.4025E−10
24	Hφ	1.2061E−05	2.5126E−05	−1.7401E−03	2.3535E−05	−1.7876E−03
25	H φ^2	−7.5954E−06	−1.1335E−06	7.8360E−04	4.9201E−05	3.0528E−04
26	H^2 φ	−2.3193E−09	−9.8886E−09	1.2612E−07	−4.5368E−08	3.6136E−07
27	H A	1.5098E−05	7.7865E−06	−1.7847E−04	−6.3914E−06	8.4818E−05
28	H A^2	−3.9864E−07	−8.1203E−07	1.0487E−05	−8.4262E−07	−3.8639E−06
29	H^2 A	−2.5997E−09	−4.0054E−10	1.9120E−08	3.8546E−09	−3.5269E−08
30	H$\sqrt{N}$	3.6813E−05	−8.7143E−06	2.8698E−04	3.6726E−04	8.6295E−04
31	H N	−8.0319E−08	1.4203E−07	3.6164E−05	−1.5490E−05	3.3162E−05
32	$H^2\sqrt{N}$	−8.2386E−09	1.3684E−09	−9.8433E−08	−6.0903E−08	−2.1210E−07
33	$\log_{10}(Pe)^2$	−2.4553E−01	9.7988E−02	3.5636E+00	1.1031E+00	1.7310E+00
34	$\log_{10}(Pe)^3$	−1.8898E−02	6.4083E−02	5.0366E−01	1.6111E−01	1.9714E−01
35	$\log_{10}(Pe)$ φ	−2.3681E−02	−2.6701E−01	4.6605E−01	1.3312E−01	5.3177E−01
36	$\log_{10}(Pe)$ φ^2	−1.6041E−02	−1.0029E−02	−2.9379E−02	1.4115E−02	−3.7244E−01
37	$\log_{10}(Pe)^2$ φ	−3.6204E−03	−4.3230E−02	7.3366E−02	4.3969E−02	−1.1342E−02
38	$\log_{10}(Pe)$ A	−1.8394E−02	−1.7428E−02	1.7073E−01	5.5187E−02	3.2277E−01
39	$\log_{10}(Pe)$ A^2	−3.1571E−04	−1.9462E−04	−8.4293E−03	−3.8041E−04	−2.5022E−02
40	$\log_{10}(Pe)^2$ A	−3.1225E−03	−3.2116E−03	1.2388E−02	5.8127E−03	1.9736E−02
41	$\log_{10}(Pe)\sqrt{N}$	−6.6441E−02	5.7831E−02	−6.4111E−01	−8.8787E−01	−9.6208E−01
42	$\log_{10}(Pe)$ N	1.5067E−03	−3.4381E−04	−1.6142E−02	4.3027E−02	−3.8777E−02
43	$\log_{10}(Pe)^2\sqrt{N}$	−6.7684E−03	9.4207E−03	−7.8682E−02	−7.2797E−02	−1.7132E−01
44	$\log_{10}(Pe)$ H	−2.7453E−04	−3.3213E−04	−2.1863E−03	−1.0735E−03	−5.0536E−03
45	$\log_{10}(Pe)$ H^2	4.3906E−08	6.3397E−08	2.5028E−07	2.1955E−07	1.6748E−07
46	$\log_{10}(Pe)^2$ H	−1.1176E−05	8.2892E−06	−9.3075E−05	−3.1761E−05	−5.0428E−04
47	B^2	−8.2131E−05	−4.0632E−05	−1.2867E−04	2.9165E−05	2.1071E−04
48	B^3	1.5771E−07	5.7824E−08	−6.8127E−07	−1.0357E−07	−1.9176E−06
49	B φ	5.6866E−04	−2.7285E−04	1.2277E−02	2.9985E−04	3.8253E−03
50	B φ^2	−3.0642E−04	1.0693E−04	−5.8833E−03	−7.3191E−04	−2.8608E−03
51	B^2 φ	−5.3247E−07	−3.5663E−07	−1.6325E−05	3.3914E−06	2.8519E−06
52	B A	−2.3665E−04	−1.4839E−04	7.3220E−04	−2.5392E−04	5.7636E−03
53	B A^2	−2.6657E−06	3.5618E−07	−4.9968E−05	1.4946E−05	−4.6964E−04
54	B^2 A	6.9611E−07	3.9815E−07	5.8551E−07	6.2671E−07	−1.1376E−05
55	B$\sqrt{N}$	−5.3407E−04	1.3634E−04	−1.3894E−02	−4.7178E−03	−1.5687E−02
56	B N	7.2165E−06	−6.8425E−06	−3.2473E−04	2.2937E−04	−4.4153E−04
57	$B^2\sqrt{N}$	1.0466E−06	1.0058E−08	4.9545E−05	5.3044E−06	5.4022E−05
58	B H	8.4486E−07	−7.3917E−07	−3.2796E−05	1.3945E−08	−4.0378E−05
59	B H^2	−3.1418E−11	2.7276E−11	4.8503E−09	−4.5214E−11	4.5791E−09
60	B^2 H	−2.5065E−09	1.3762E−09	4.7238E−08	1.2025E−09	7.5659E−08
61	B $\log_{10}(Pe)$	−1.4610E−03	3.1736E−03	4.6317E−02	1.1285E−02	4.4855E−02
62	B $\log_{10}(Pe)^2$	−1.7174E−04	4.4974E−04	3.5966E−03	1.4457E−03	2.7706E−03
63	B^2 $\log_{10}(Pe)$	1.1951E−06	−2.8921E−06	−7.4600E−05	−5.9367E−06	−8.5610E−05
64	1	1.0667E+00	1.0766E+00	−7.8374E−01	3.0762E+00	−1.4270E+00

References

[1] Canadian GeoExchange Coalition. The state of the Canadian geothermal heat pump industry 2011. Ind Market Anal 2012.

[2] ASHRAE Handbook 2007. HVAC applications. Atlanta, Georgia: American Society of Heating, Refrigerating and Air-Conditioning Engineers; 2011.

[3] Chiasson AD, Rees SJ, Spitler JD. A preliminary assessment of the effects of groundwater flow on closed-loop ground source heat pump systems. ASHRAE Trans 2000;106(1):380–93.

[4] van Meurs G. Seasonal heat storage in soil. Thesis. Netherlands: Dept. of Applied Physics, University of Technology Delft; 1986.

[5] Eskilson P. Thermal analysis of heat extraction boreholes. Ph.D. Thesis. Lund, Sweden: Lund University; 1987.

[6] Claesson J, Hellström G. Analytical studies of the influence of regional groundwater flow on the performance of borehole heat exchangers. In: Presented at the Proceedings of the 8th international conference on thermal energy storage, Terrastock 2000, Stuttgart, Germany; 2000. p. 195–200.
[7] Sutton MG, Nutter DW, Couvillion RJ. A ground resistance for vertical bore heat exchangers with groundwater flow. J Energy Resour Technol 2003;125(3):183.
[8] Diao N, Li Q, Fang Z. Heat transfer in ground heat exchangers with groundwater advection. Int J Therm Sci Dec. 2004;43(12):1203–11.
[9] Molina-Giraldo N, Blum P, Zhu K, Bayer P, Fang Z. A moving finite line source model to simulate borehole heat exchangers with groundwater advection. Int J Therm Sci Dec. 2011;50(12):2506–13.
[10] Capozza A, De Carli M, Zarrella A. Investigations on the influence of aquifers on the ground temperature in ground-source heat pump operation. Appl Energy 2013;107:350–63.
[11] Katsura T, Nagano K, Takeda S, Shimakura K. Heat transfer experiment in the ground with ground water advection. In: Proceedings of the 10th Energy conservation thermal energy storage conference. Ecostock; 2006. p. 1–27.
[12] Składzień J, La MH-D, Fic A. Thermal analysis of vertical ground exchangers of heat pumps. Heat Transf Eng 2006;27(2):2–13.
[13] Nam Y, Ooka R, Hwang S. Development of a numerical model to predict heat exchange rates for a ground-source heat pump system. Energy Build 2008;40(12):2133–40.
[14] Lee CK, Lam HN. A modified multi-ground-layer model for borehole ground heat exchangers with an inhomogeneous groundwater flow. Energy 2012;47(1):378–87.
[15] Choi JC, Park J, Lee SR. Numerical evaluation of the effects of groundwater flow on borehole heat exchanger arrays. Renew Energy 2013;52:230–40.
[16] Fan R, Jiang Y, Yao Y, Shiming D, Ma Z. A study on the performance of a geothermal heat exchanger under coupled heat conduction and groundwater advection. Energy Nov. 2007;32(11):2199–209.
[17] Hecht-Méndez J, de Paly M, Beck M, Bayer P. Optimization of energy extraction for vertical closed-loop geothermal systems considering groundwater flow. Energy Convers Manag Feb. 2013;66:1–10.
[18] Nield DA, Bejan A. Convection in porous media. Springer; 2006.
[19] Molina-Giraldo N, Bayer P, Blum P. Evaluating the influence of thermal dispersion on temperature plumes from geothermal systems using analytical solutions. Int J Therm Sci Jul. 2011;50(7):1223–31.
[20] Chiasson A, O'Connell A. New analytical solution for sizing vertical borehole ground heat exchangers in environments with significant groundwater flow: parameter estimation from thermal response test data. HVAC&R Res Dec. 2011;17(6):1000–11.
[21] Wagner V, Bayer P, Kübert M, Blum P. Numerical sensitivity study of thermal response tests. Renew Energy May 2012;41:245–53.
[22] Lu X, Ren T, Gong Y. Experimental investigation of thermal dispersion in saturated soils with one-dimensional water flow. Soil Sci Soc Am J Nov. 2009;73(6):1912–20.
[23] Carslaw HS, Jaeger JC. Heat conduction in solids. Oxford: Claremont Press; 1947.
[24] Lamarche L. Short-term behavior of classical analytic solutions for the design of ground-source heat pumps. Renew Energy 2013;57:171–80.
[25] Marcotte D, Pasquier P. On the estimation of thermal resistance in borehole thermal conductivity test. Renew Energy 2008;33:2407–15.
[26] Pasquier P, Marcotte D. Joint use of quasi-3D TRCM and spectral method to simulate ground heat exchanger. Geothermics 2014;51:281–99.
[27] Zeng H, Diao N, Fang Z. Heat transfer analysis of boreholes in vertical ground heat exchangers. Int J Heat Mass Transf Nov. 2003;46(23):4467–81.
[28] Lamarche L, Beauchamp B. A new contribution to the finite line-source model for geothermal boreholes. Energy Build Feb. 2007;39(2):188–98.
[29] Ingersoll L, Zobel O, Ingersoll A. Heat conduction with engineering, geological and other applications. New-York: McGraw-Hill; 1954.
[30] Deerman JD, Kavanaugh SP. Simulation of vertical U-tube ground coupled heat pump systems using the cylindrical heat source solution. ASHRAE Trans 1991;97(1):287–95.
[31] Kavanaugh SP, Rafferty K. Ground-source heat pumps – design of geothermal systems for commercial and institutional buildings; 1997.
[32] Bernier MA. Ground-coupled heat pump system simulation. ASHRAE Trans 2001;107(1):605–16.
[33] Philippe M, Bernier M, Marchio D. Validity ranges of three analytical solutions to heat transfer in the vicinity of single boreholes. Geothermics Dec. 2009;38(4):407–13.
[34] Comsol multiphysics 4.2a. Comsol Inc.; 2011.
[35] Yavuzturk C. Modeling of vertical ground loop heat exchangers for ground source heat pumps systems. United States: Oklahoma State University; 1999.
[36] Bernier MA, Pinel P, Labib R, Paillot R. A multiple load aggregation algorithm for annual hourly simulations of GCHP systems. HVAC&R Res 2004;10(4):471–87.
[37] Lamarche L. A fast algorithm for the hourly simulations of ground-source heat pumps using arbitrary response factors. Renew Energy 2009;34(10):2252–8.
[38] Marcotte D, Pasquier P. Fast fluid and ground temperature computation for geothermal ground-loop heat exchanger systems. Geothermics Dec. 2008;37(6):651–65.
[39] Fossa M. The temperature penalty approach to the design of borehole heat exchangers for heat pump applications. Energy Build Jun. 2011;43(6):1473–9.
[40] Capozza A, De Carli M, Zarrella A. Design of borehole heat exchangers for ground-source heat pumps: a literature review, methodology comparison and analysis on the penalty temperature. Energy Build Dec. 2012;55:369–79.
[41] Bernier MA, Chahia A, Pinel P. Long-term ground-temperature changes in geo-exchange systems. ASHRAE Trans 2008;114(2):342–50.
[42] Reif F. Fundamentals of statistical and thermal physics. McGraw-Hill; 1965.
[43] Guaraglia DO, Pousa JL, Kruse EE, Mayosky MA. A rotary thermal probe for measuring groundwater velocity,. Instrum Sci Technol 2009;37:303–18.
[44] Patterson BM, Annable MD, Bekele EB, Furness AJ. On-line groundwater velocity probe: laboratory testing and field evaluation. J Contam Hydrol 2010;117(1–4):109–18.
[45] Robert F, Gosselin L. New methodology to design ground couple heat pumps systems based on total cost minimization. Appl Therm Eng 2014;62(2):481–91.